Cellulose synthase complexes display distinct dynamic behaviors during xylem transdifferentiation

Yoichiro Watanabe[a,b,1], Rene Schneider[c,d,1], Sarah Barkwill[b], Eliana Gonzales-Vigil[b], Joseph L. Hill Jr.[e,2], A. Lacey Samuels[a,3,4], Staffan Persson[c,3,4], and Shawn D. Mansfield[b,3,4]

[a]Department of Botany, University of British Columbia, Vancouver, BC V6T 1Z4, Canada; [b]Department of Wood Science, University of British Columbia, Vancouver, BC V6T 1Z4, Canada; [c]School of Biosciences, University of Melbourne, Parkville VIC 3010, Australia; [d]Max Planck Institute for Molecular Plant Physiology, 14476 Potsdam, Germany; and [e]Department of Biochemistry and Molecular Biology, Pennsylvania State University, University Park, PA 16802

Edited by Deborah J. Delmer, Emeritus University of California, Davis, CA, and approved May 11, 2018 (received for review February 6, 2018)

In plants, plasma membrane-embedded CELLULOSE SYNTHASE (CESA) enzyme complexes deposit cellulose polymers into the developing cell wall. Cellulose synthesis requires two different sets of CESA complexes that are active during cell expansion and secondary cell wall thickening, respectively. Hence, developing xylem cells, which first undergo cell expansion and subsequently deposit thick secondary walls, need to completely reorganize their CESA complexes from primary wall- to secondary wall-specific CESAs. Using live-cell imaging, we analyzed the principles underlying this remodeling. At the onset of secondary wall synthesis, the primary wall CESAs ceased to be delivered to the plasma membrane and were gradually removed from both the plasma membrane and the Golgi. For a brief transition period, both primary wall- and secondary wall-specific CESAs coexisted in banded domains of the plasma membrane where secondary wall synthesis is concentrated. During this transition, primary and secondary wall CESAs displayed discrete dynamic behaviors and sensitivities to the inhibitor isoxaben. As secondary wall-specific CESAs were delivered and inserted into the plasma membrane, the primary wall CESAs became concentrated in prevacuolar compartments and lytic vacuoles. This adjustment in localization between the two CESAs was accompanied by concurrent decreased primary wall CESA and increased secondary wall CESA protein abundance. Our data reveal distinct and dynamic subcellular trafficking patterns that underpin the remodeling of the cellulose biosynthetic machinery, resulting in the removal and degradation of the primary wall CESA complex with concurrent production and recycling of the secondary wall CESAs.

cellulose | primary cell wall | secondary cell wall | cellulose biosynthesis | xylem transdifferentiation

Cellulose is the most abundant biopolymer on Earth and is a major constituent of the plant cell wall (1). It is also of immense importance to a range of human uses and industries, including fiber, fuel, textile, fodder, and specialty chemicals (2). Cellulose is a homopolymer composed of long chains of 1,4-β–linked glucose molecules (3). The polymeric chains are largely arranged in parallel orientation that allows inter- and intrachain hydrogen bonds that ultimately form cellulose microfibrils that contain domains of high crystallinity (4, 5). The microfibrils display high tensile strength and provide the support for the structural integrity of the cell-wall types in plants. During cell division and growth, the orientation of primary cell wall (PCW) cellulose microfibrils directs cell expansion by acting as the main load-bearing component that resists the turgor pressure driving growth (6). Once cell expansion ceases, specialized cell types produce thick and chemically distinct secondary cell walls (SCWs) that contain a larger portion of cellulose than PCWs. SCWs provide the structural strength required for fibers to hold the plant upright and reinforce vessels and tracheary elements to resist the negative pressures associated with water transport (7).

Cellulose is generated by a family of integral membrane glycosyltransferases called "CELLULOSE SYNTHASES" (CESAs), of which there are 10 (AtCESA1–10) in *Arabidopsis thaliana* (8). In vascular plants, the CESAs oligomerize, forming six-lobed rosette structures known as "cellulose synthase complexes" (CSCs) (9), estimated to contain between 18 and 24 CESAs (10–12). Oligomers are thought to form in the Golgi and *trans*-Golgi network (TGN) (13) before the assembled complexes are delivered to the plasma membrane, possibly via vesicles called "small CESA-containing compartments" (SmaCCs) (14) or "microtubule-associated CESA compartments" (MASCs) (15). At the plasma membrane, active CESAs utilize cytoplasmic UDP-glucose as a substrate to synthesize glucan chains that are extruded into the apoplast (16–18). The catalytic activity of CESAs and the aggregation of cellulose into microfibrils are believed to propel the CSCs through the plasma membrane (19–21). Thus the speed of a CSC at the plasma membrane is routinely used as proxy for its catalytic activity (19, 22).

It is widely accepted that a CSC needs three distinct isoforms to function and that the specific isoforms differ depending on whether the CSCs are forming PCWs or SCWs. For example, mutant studies and coexpression data in *Arabidopsis* clearly demonstrate that the PCW CSCs consist of AtCESA1, AtCESA3, and one of the partially redundant AtCESA6-like CESAs (AtCESA2, AtCESA5, AtCESA6, and AtCESA9) (23–25), while AtCESA4, AtCESA7, and AtCESA8 are strictly associated with and required for the production of SCWs (26). Given the functional divergence and expression relationships of the CESAs, one might assume that PCW

Significance

Cellulose, the most abundant biopolymer on earth, is the major constituent of plant cell walls and is ubiquitously used by industry. This biopolymer is made by plasma membrane-localized CELLULOSE SYNTHASE (CESA) enzymes. To transit from deposition of a growing primary cell wall to a strong secondary cell wall, xylem cells must remodel the CESA machinery to express a new set of CESA isoforms specific to secondary cell wall synthesis. We outline a detailed framework for how this change in cellulose synthesis occurs. Our work provides the principles for how plants change their capacity to produce cellulose and therefore plant biomass.

Author contributions: A.L.S., S.P., and S.D.M. designed research; Y.W., R.S., S.B., and E.G.-V. performed research; J.L.H. contributed new reagents/analytic tools; Y.W. and R.S. analyzed data; and Y.W., R.S., A.L.S., S.P., and S.D.M. wrote the paper.

The authors declare no conflict of interest.

This article is a PNAS Direct Submission.

See Commentary on page 6882.

[1]Y.W. and R.S. contributed equally to this work.

[2]Present address: Department of Horticulture, Michigan State University, East Lansing, MI 48824.

[3]A.L.S., S.P., and S.D.M. contributed equally to this work.

[4]To whom correspondence may be addressed. Email: annelacey.samuels@botany.ubc.ca, staffan.persson@unimelb.edu.au, or shawn.mansfield@ubc.ca.

This article contains supporting information online at www.pnas.org/lookup/suppl/doi:10.1073/pnas.1802113115/-/DCSupplemental.

Published online June 5, 2018.

CSCs are replaced by SCW CSCs (e.g., during the development of xylem cells). However, it was also suggested that PCW and SCW CESAs can co-occur in the same CSCs (27). Nevertheless, the principles behind the CSC remodeling are unknown, and we therefore do not understand if both PCW and SCW CESAs are present together at the plasma membrane or if and how PCW CSCs are removed as SCW synthesis proceeds.

As SCWs are deposited around cells that typically are situated deep in plant tissues, studies of the transition from PCW to SCW synthesis have been limited. This inherent location limits the ability to carry out live-cell imaging with high enough resolution to distinguish individual CSCs and intracellular compartments in these cells (28). To overcome this, an experimental system can be used in which epidermal cells of the hypocotyls of dark-grown *Arabidopsis* seedlings are induced to transdifferentiate into SCW-producing protoxylem tracheary element cells due to the expression of a master transcription factor, VASCULAR-RELATED NAC-DOMAIN7, linked to an inducible glucocorticoid receptor system (VND7-GR) (29). This system allows SCW biosynthesis to be observed easily with high resolution (30–33). Sum-frequency generation vibrational spectroscopy demonstrated that the cellulose properties of these induced SCWs are consistent with the properties of native tracheary element SCWs (31). Microarray data indicate that PCW *CESA* genes were down-regulated following VND7 induction, while the expression of SCW *CESA* genes increased (34, 35). However, how the cell coordinates the PCW and SCW CESA proteins at the plasma membrane during xylem vessel development remains to be resolved. We generated a system in which we could directly study the coordination of the two CSCs. We found that the PCW and SCW CSCs co-occur during certain stages of xylem vessel development but maintain different levels of catalytic activity. In addition, the vesicle traffic of CSCs changes during the transition to mobilize PCW CESAs for degradation in the lytic vacuole, while the SCW CESAs are actively delivered and maintained at the cell membrane.

Results

PCW CESAs Become Internalized During Xylem Vessel Development. To elucidate how plant cells transition from making PCWs to SCWs, we crossed VND7-inducible *Arabidopsis* plants expressing fluorescently tagged PCW CESAs, *proCESA6::tdTomato-CESA6* (36), and tubulin, *proCaMV35s::YFP-TUA5* (37). Three-day-old etiolated seedlings of the progeny were induced with dexamethasone in DMSO (29). In noninduced DMSO controls, the tdTomato-CESA6 migrated along linear trajectories that were evenly dispersed across the plasma membrane and were clearly visible in cytosolic compartments such as Golgi and SmaCCs (Fig. 1*A* and *SI Appendix*, Fig. S1*A*). Following induction, the early transition from PCWs to SCWs was defined by the reorganization of cortical microtubules into diffuse bands that mark areas where the onset of SCW synthesis will occur (30, 32). The tdTomato-CESA6 trajectories followed the microtubule reorganization and maintained a speed of ∼199 ± 40 nm/min (n = 334 CSCs in 11 cells) during the transition (Fig. 1 *B–D*). Indeed, kymographs of the tdTomato-CESA6 signal showed smooth, continuous lines characteristic of catalytically active plasma membrane-localized complexes in both preinduction and early-transition stages (Fig. 1*C*). During the subsequent transition phase, defined here as midtransition (Fig. 1*B*), kymograph analysis showed that the steadily moving plasma membrane-located tdTomato-CESA6 signal became less prevalent, and instead the CESAs were increasingly observed to move erratically (Fig. 1*C* and Movie S1) and were less well coordinated with the microtubule bands (Fig. 1 *B–D*). This movement was highly reminiscent of that reported for the SmaCCs/MASCs (14, 15). The erratically moving tdTomato-CESA6 foci were also observable during the late-transition stage but were more difficult to discern due to high uniform background signal that most likely emanated from the vacuole (Fig. 1 *B–D*).

PCW and SCW CESAs Briefly Co-Occur but Have Different Velocities at the Plasma Membrane During Xylem Vessel Transdifferentiation. To visualize PCW and SCW CESAs simultaneously during the transition, we generated *Arabidopsis* plants expressing *proCESA6::tdTomato-CESA6* and a fluorescently tagged AtCESA7 (*proCESA7::YFP-CESA7*) (30) in the VND7-GR–inducible system. Before VND7 induction, we did not observe any YFP-CESA7 signal in the cells, whereas clear tdTomato-CESA6 signal was detected as described above (Fig. 2*A*, pretransition). During the early phase of transition, a clear YFP-CESA7 signal appeared in intracellular compartments in close proximity to the plasma membrane, in ring-shaped Golgi bodies, and in SmaCCs (Fig. 2*A*, arrowheads). As the transition progressed, motile YFP-CESA7 appeared at the plasma membrane and tracked along trajectories similar to those of tdTomato-CESA6 (Figs. 2*A* and 3*A* and Movie S2). However, this developmental window, showing plasma membrane localization of both tdTomato-CESA6 and YFP-CESA7, was relatively short-lived and was maintained for a maximum of 1 h, indicating that the PCW CSCs stopped being delivered to the plasma membrane. We corroborated this hypothesis through photobleaching experiments in which we found that the recovery of the tdTomato-CESA6 fluorescence was substantially delayed compared with the recovery of the YFP-CESA7 fluorescence (Fig. 2 *B–D*, arrowheads and Movie S3). Kymograph analysis along these bands revealed steadily moving YFP-CESA7 foci appearing in bleached areas, indicating the delivery of active YFP-CESA7–containing CSCs to the plasma membrane (Fig. 2*C*, arrows). The tdTomato-CESA6 signal was subsequently removed from the plasma membrane and was observed only within bright intracellular puncta (Fig. 2*A*, arrows). The transition phase was considered complete when only YFP-CESA7, but no tdTomato-CESA6, fluorescence was evident as distinct foci at or in close proximity to the plasma membrane (Fig. 2*A*).

The co-occurrence of both PCW and SCW CESAs in the same cell permitted detailed analysis of their relative behaviors (Fig. 3*A*). Kymograph analyses indicated that the tdTomato-CESA6 and YFP-CESA7 moved with different speeds (Fig. 3 *B* and *C*). Indeed, during midtransition the tdTomato-CESA6 moved with a speed of 251 ± 19 nm/min (n = 128 CSCs in four cells from three seedlings), while the YFP-CESA7 moved significantly faster (430 ± 62 nm/min; n = 682 CSCs in 10 cells from three seedlings; $P < 0.0001$, Welch's unpaired t test) (Fig. 3*D*). These data show that the PCW and SCW CESAs co-occur at the plasma membrane for only a short while and that the two CSCs move with different speeds. Hence, we conclude that the tdTomato-CESA6 CESAs move independently of the YFP-CESA7 CESAs (Fig. 3 *C* and *D*), although the two CESAs track along common paths.

The Cellulose Synthesis Inhibitor Isoxaben Affects PCW but Not SCW CESA Dynamics. The PCW CSC in *Arabidopsis* is highly sensitive to the cellulose synthesis inhibitor isoxaben (38). However, cellulose synthesis in grasses does not show the same type of sensitivity (39), and it is unclear to what degree SCW cellulose synthesis is affected by the inhibitor. To assess how isoxaben affected the dynamic behavior of tdTomato-CESA6 and YFP-CESA7, we first grew the VND7-inducible seedlings on 0.5× Murashige and Skoog (MS) medium for 2 d in the dark and then transferred them to medium containing 200 nM isoxaben for another day (Fig. 4*A*). Interestingly, whereas the noninduced seedlings showed severe cell swelling, the VND7-induced seedlings showed less swelling and were able to produce clear secondary wall bands (Fig. 4 *A* and *B*). Moreover, cell-wall staining using the cellulose-binding dye Scarlet S4B (40) revealed clear cellulose bands in the VND7-induced seedlings in both the absence and presence of isoxaben (Fig. 4*C*). To assess how isoxaben influenced CESA dynamics, we

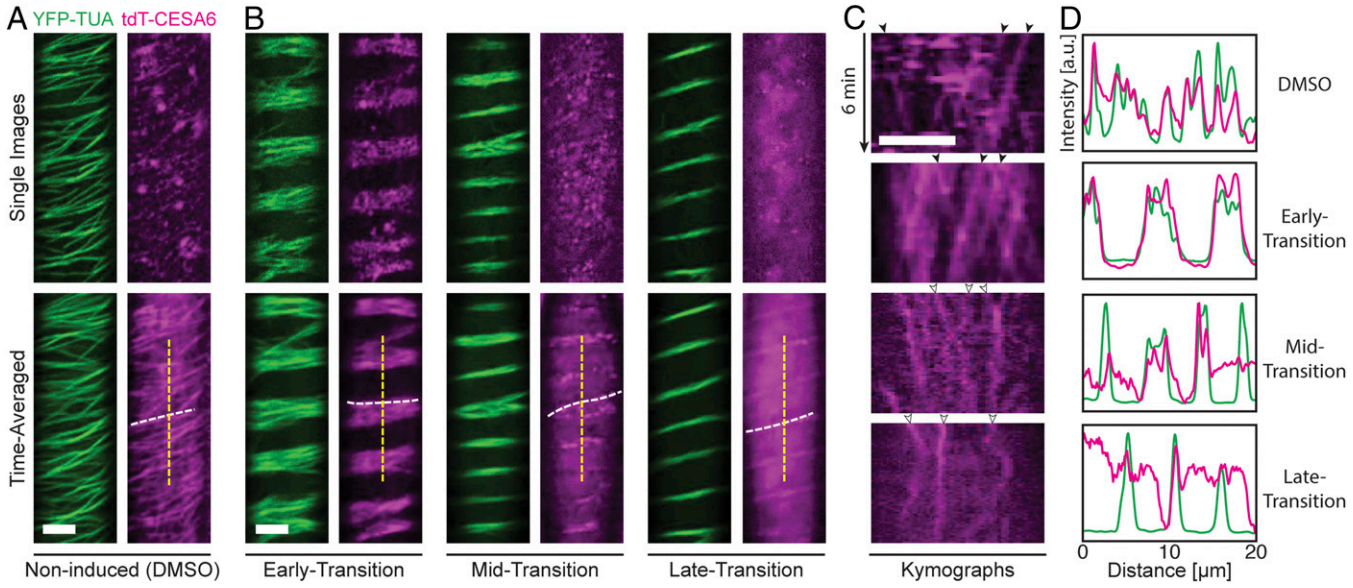

Fig. 1. Plasma membrane-localized primary CESAs transiently co-occur with forming microtubule (MT) bands and are subsequently depleted during SCW formation. (*A*) Three-day-old etiolated hypocotyl epidermal cells expressing YFP-TUA5 (YFP-TUA; green) and tdTomato-CESA6 (tdT-CESA6; magenta) in the VND7-inducible background. Shown are single (*Upper*) and time-averaged (*Lower*) images of the fluorescent signals. Noninduced seedlings show transverse microtubules (MTs) aligned with migrating tdT-CESA6 at the plasma membrane. (Scale bar: 5 μm.) (*B*) During early transition, the MTs of induced seedlings undergo reorientation into diffuse bands, which causes similar tdT-CESA6 reorganization. During midtransition, some tdT-CESA6 signal is maintained in the plasma membrane, but bright round intracellular foci were also prominent. The late-transition stage revealed no tdT-CESA6 signal at the plasma membrane but instead abundant and diffuse intracellular signal. (Scale bar: 5 μm.) (*C*) Kymographs along the dotted lines in *A* and *B*. In noninduced and early transition (top two kymographs), arrowheads indicate stable movement of catalytically active tdT-CESA6 in the plasma membrane; in mid- and late transition (bottom two kymographs), empty arrowheads indicate erratically moving intracellular compartments. (Scale bar: 5 μm.) (*D*) Fluorescence intensity plots of tdT-CESA6 (pink) and YFP-TUA (green).

first observed the tdTomato-CESA6 line and found, similar to previous studies, that the fluorescent foci disappeared from the plasma membrane and accumulated in internal SmaCCs/MASCs (Fig. 4*D*). We next examined the behavior of YFP-CESA7 in the VND7-induced seedlings. In contrast to tdTomato-CESA6, YFP-CESA7 maintained steady movement at the plasma membrane, and there were no differences in speed before and after isoxaben treatment (Fig. 4 *E* and *F*). We furthermore confirmed that the cellulose content was unaltered in the VND7-induced seedlings after isoxaben treatment, confirming that SCW cellulose synthesis is not affected by isoxaben (Fig. 4*G*). Hence, isoxaben might be used to perturb PCW cellulose synthesis while maintaining SCW cellulose synthesis intact.

PCW CESAs Are Internalized and Trafficked to Late Endosomes/Prevacuolar Compartments During Mid to Late Xylem Vessel Development Stages. The gradual loss of tdTomato-CESA6 signal at the plasma membrane indicated that it might be degraded. To assess this, we examined deeper optical sections within cells during the various stages of transdifferentiation to elucidate the nature of the intracellular tdTomato-CESA6 localization (Fig. 5*A*). Intracellular CESA compartments were defined as outlined in *SI Appendix*, Fig. S1. During the pretransition stage, we observed cytosolic tdTomato-CESA6–labeled compartments including Golgi (arrowheads) and SmaCCs (Fig. 5*A*, pretransition, yellow arrows). Once the YFP-CESA7 became visible, the two fluorescently labeled CESAs coincided in both Golgi and SmaCCs (Fig. 5 *A*–*C*, early transition and Movie S4). As SmaCCs might be involved in both the delivery of CESAs to the plasma membrane and their endocytosis/recycling, we cannot determine if these dual-labeled SmaCCs are anterograde or retrograde in nature. However, as the delivery of tdTomato-CESA6 stops once YFP-CESA7 is at the plasma membrane (Fig. 2*B*), these SmaCCs are most likely compartments involved in CESA endocytosis and/or recycling. Interestingly, during the mid-stages of the process, the Golgi-located tdTomato-CESA6 signal started to fade (arrowheads), and bright distinct puncta that did not coincide with YFP-CESA7 became apparent (white arrows; Fig. 5 *A* and *B* and Movie S5). These compartments were distinctly different from the YFP-CESA7 SmaCCs or tdTomato-CESA6 SmaCCs seen at earlier time points, as they were slightly larger and brighter than the SmaCCs (*SI Appendix*, Fig. S1*B*). By late transition, no Golgi-localized tdTomato-CESA6 was detectable, and there was a concurrent increase in diffuse tdTomato-CESA6 signal from the vacuole (Fig. 5 *A* and *B* and Movie S6). Once the transition was complete, only the diffuse vacuolar tdTomato-CESA6 signal remained (Fig. 5*A*, posttransition). We quantified these shifts in localization using colocalization analysis of tdTomato-CESA6 and YFP-CESA7 (Fig. 5*C*). Consistent with our observations, colocalization was highest during early transition, when both proteins were present in the Golgi and SmaCCs, and decreased steadily at later time points when the localization of tdTomato-CESA6 shifted to discrete puncta and to the vacuoles (Fig. 5*C*).

The appearance of distinct tdTomato-CESA6–containing compartments and the subsequent vacuolar signal during the mid- and late-transition phases prompted us to hypothesize that CESA6 was trafficked through prevacuolar compartments (PVCs)/multivesicular bodies (MVBs) to become degraded. If this is true, we expected that the number of puncta containing tdTomato-CESA6 exclusively would increase during the transition. Therefore we measured the divergence of the tdTomato-CESA6 and YFP-CESA7 signals by quantifying loss of co-occurrence of tdTomato-CESA6– and YFP-CESA7–labeled compartments at different stages of transition (*SI Appendix*, Fig. S2). At early transition, 39 ± 12% (mean ± SD, $n = 20$ cells) of SmaCCs containing tdTomato-CESA6 did not co-occur with YFP-CESA7 fluorescence. This percentage remained the same at midtransition with 45 ± 6% of tdTomato-CESA6 SmaCCs without YFP signal. However, by late transition, 55 ± 10% of the tdTomato-CESA6–labeled compartments contained only red fluorescence and hence no YFP-CESA7 (*SI Appendix*, Fig. S2*C*). To test if these tdTomato-CESA6–enriched

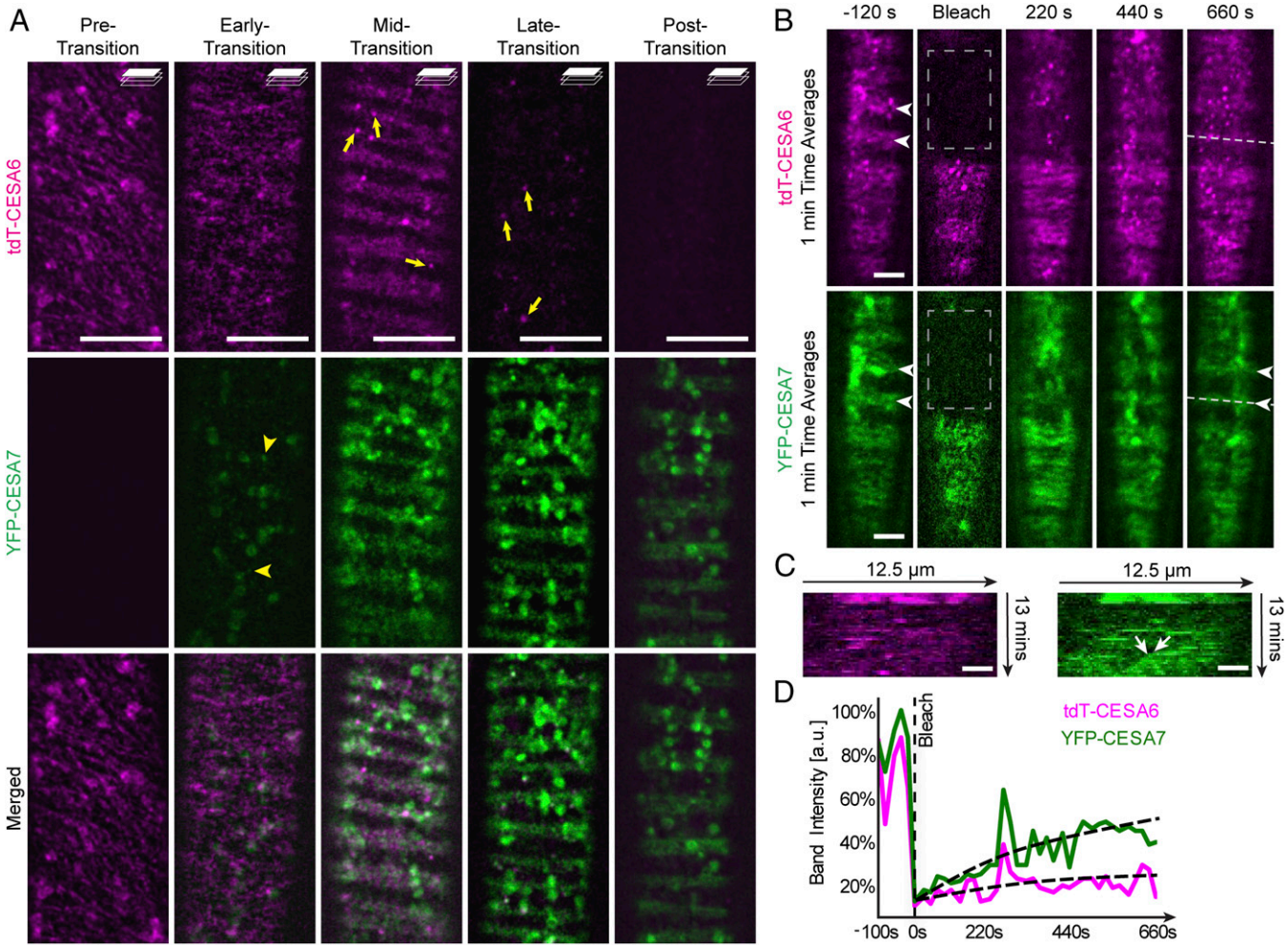

Fig. 2. PCW CSCs briefly coexist with and are subsequently replaced by SCW complexes. Shown are 3-d-old etiolated hypocotyl cells expressing YFP-CESA7 (green) and tdTomato-CESA6 (tdT-CESA6; magenta) in the VND7-inducible background. (*A*) Pretransition: tdTomato-CESA6–containing CSCs are visible at the plasma membrane as a diffuse pattern in which they migrate along linear trajectories. Early transition: YFP-CESA7–containing CSCs begin to appear in intracellular compartments including SmaCCs (arrowheads), while tdT-CESA6 remains at the plasma membrane. Midtransition: both YFP-CESA7 and tdT-CESA6 appear at the plasma membrane and steadily migrate along diffuse bands. Here, tdT-CESA6s begin to appear in distinct and bright intracellular compartments (arrows) that typically coincide with cortical microtubule bands (see also Fig. 1 *B* and *D*). Late transition: Only YFP-CESA7 signal was observed at the plasma membrane, while tdT-CESA6 was seen only within cortical compartments (arrows). Posttransition: tdT-CESA6 fluorescence is no longer seen associated with distinct cortical compartments, and only YFP-CESA7 signal is observed as distinct foci at the plasma membrane or cortical compartments. (Scale bars: 10 µm.) (*B*) Time-average images of induced dual-labeled tdT-CESA6 and YFP-CESA7 before and after photobleaching. Primary and secondary CSCs coexist in bands before photobleaching (arrowheads). tdT-CESA6 fails to be recruited to the bleached region after 11 min, whereas YFP-CESA7 reappears at the location of the band (arrowheads). (Scale bars: 5 µm.) (*C*) Kymographs along the dashed lines in *B* reveal that recovery of tdT-CESA6 fluorescence is largely due to vesicles moving in the cytoplasm, while YFP-CESA7 fluorescence reappears also in the form of migrating dots (arrows) moving along the previously bleached bands indicating newly delivered YFP-CESA7–containing CSCs. (Scale bars: 2 µm.) (*D*) Fluorescence recovery curves reveal slow recovery of tdT-CESA6 (0.012 ± 0.005 a.u./s) while YFP-CESA7 fluorescence recovers substantially faster (0.053 ± 0.005 a.u./s, mean ± SD, measured from five recovery curves; $P < 0.0001$, Welch's unpaired *t* test).

compartments were PVC/MVBs, we treated plants at the midtransition stage with wortmannin (*SI Appendix*, Fig. S3), a pharmaceutical agent known to block CESA endocytosis (41) and trafficking to the lytic vacuole by inhibiting phosphatidylinositol-phosphate-3 kinases (42). In cells treated with wortmannin, the tdTomato-CESA6–containing puncta still formed. However, in the treated cells, unlike DMSO-treated controls at the same time point, we did not observe any tdTomato-CESA6 vacuolar signal (*SI Appendix*, Fig. S3), indicating that wortmannin treatment inhibited tdTomato-CESA6 trafficking to the vacuole.

PCW CESAs Are Degraded as SCW CESAs Accumulate During Xylem Tracheary Element Transdifferentiation. Although we show that tdTomato-CESA6 disappears from the plasma membrane and appears in the lytic vacuoles, while YFP-CESA7 accumulates rapidly during the transition from PCW to SCW synthesis, the question remains whether the other CESAs behave accordingly. To determine if the other PCW-specific CESAs, i.e., CESA1 and CESA3, are degraded while the SCW-specific CESAs CESA4, CESA7, and CESA8 are accumulating, we collected protein extracts during the transdifferentiation and performed Western blots using antibodies specific for the different CESA isoforms (Fig. 5*D*) (43, 44). We used samples from wild-type VND7-GR-VP16 that were noninduced or were induced for 6 h (early transition), 12 h (midtransition), 18 h (late transition), and 24 h (posttransition). Consistent with our confocal data, the PCW CESA protein abundance decreased steadily in a concerted fashion, while the SCW-specific CESAs accumulated over time (Fig. 5*D*). These data therefore support our hypothesis that the

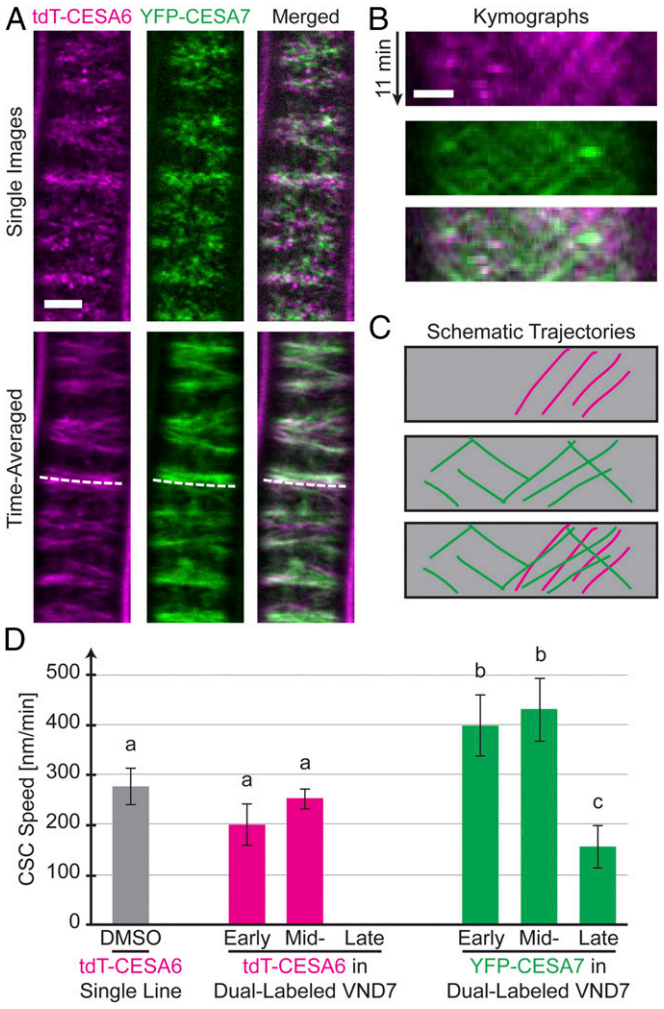

Fig. 3. PCW CSCs move independently of SCW CSCs during xylem formation. Shown are 3-d-old etiolated hypocotyl cells expressing YFP-CESA7 (green) and tdTomato-CESA6 (tdT-CESA6; magenta) in the VND7-inducible background. (*A*) Single (*Upper*) and time-averaged (*Lower*) images of the fluorescent signals. For a short period during transdifferentiation, migratory PCW and SCW CESAs co-occur along microtubule (MT) bands. (Scale bar: 5 μm.) (*B*) Kymograph plots along the dotted lines in *A* show clear differences in the speed of tdT-CESA6 and YFP-CESA7 on the same MT bundle. (Scale bar: 2 μm.) (*C*) Schematic representation of tdT-CESA6 and YFP-CESA7 trajectories, respectively, present in *B*. (*D*) CSC speed measurements in noninduced tdT-CESA6 (gray bar), VND7-induced double-labeled tdT-CESA6 (magenta bars), and YFP-CESA7 (green bars) seedlings. Groups were assigned by significant statistical differences based on Welch's unpaired *t* test ($P < 0.05$ between groups; number of measured tdT-CESA6 foci: 310 in noninduced cells and 334, 128, and 0 in induced cells at the three stages; YFP-CESA7 foci: 405, 682, and 457 in induced cells at the three stages).

PCW CESAs are targeted to the vacuole for degradation during transdifferentiation.

Discussion

The transition from PCW to SCW synthesis represents a major shift in cellular developmental processes including transcription and posttranslation modifications (34, 35). A general shift from PCW to SCW *CESA* expression has been well documented via transcriptome analysis (23, 34). However, the brief and highly regulated nature of the distinct transitional phases of this major developmental modification has made it very difficult to visualize the process. Here, we show in detail the dynamic change in PCW and SCW cellulose synthesis and demonstrate how PCW and SCW CESAs are coordinated during the differentiation of protoxylem tracheary elements. During transition, PCW CESAs are no longer delivered to the plasma membrane and instead are selectively targeted into distinct compartments for transport to the lytic vacuole. This all occurs while SCW-specific CESAs are synthesized, accumulate within intracellular compartments, and are delivered to the plasma membrane.

The selective targeting of PCW CESAs into a distinctive set of intracellular compartments and finally to the lytic vacuole hints at a mechanism involving protein modification through phosphorylation or ubiquitination. Indeed, selective inactivation of plasma membrane protein by endocytosis and degradation via ubiquitination has been well characterized (45) and has been demonstrated for several plasma-membrane proteins including the auxin-efflux protein PIN2 (46) and the boron carrier BOR1 (47). Interestingly, CESAs have several conserved phosphorylation sites (48) which have been shown not only to affect the activity of CESAs (49–52) but also to cause the selective degradation of CESAs via a proteasome pathway (53).

The formation of prevacuolar CESA6 compartments during wortmannin treatment and the disappearance of Golgi signal imply that delivery of the PCW CESAs to the vacuole may come from intracellular compartments, including Golgi and the TGN. However, this does not exclude the possibility that CESAs are targeted for degradation while still at the plasma membrane. Another plasma membrane protein, PIN2, that parallels CESAs in terms of trafficking (46, 54), has been shown to be monoubiquitinated at the plasma membrane before being polyubiquitinated at the TGN and targeted to the vacuole (55). Previous work has shown that CESAs are delivered, in part, via a TGN-associated pathway, as shown by the presence and accumulation of CESA3 within the TGN (15). Since the TGN acts as an important sorting hub for endocytosis, exocytosis, and recycling (56), it is tempting to speculate that a similar pathway exists in which CESAs are monoubiquitinated, marking them for endocytosis, at the plasma membrane and are polyubiquitinated once in TGN, which would target them for degradation. Indeed, this may explain our observation of compartments containing both tdTomato-CESA6 and YFP-CESA7 even at late stages of transition, as these may be TGNs that are involved in targeting CESA6 for degradation while transporting/recycling CESA7 to the plasma membrane. However, further work including identifying the distinct tdTomato-CESA6 compartments with endomembrane markers such as the TGN markers VTI12 and VHA-a1 (57, 58) and the PVC/late endosomal marker ARA7/RabF2B (59), is required to conclusively support our hypothesis of PCW CESA trafficking to the vacuole via the TGN and PVC.

It is well established that two distinct sets of CESAs are required for the production of PCW and SCW cellulose (1). However, our data indicate that there is a brief period when both PCW and SCW CESAs concurrently contribute to cellulose production within SCW domains. As well, given the differences in their velocities and their sensitivities to isoxaben, PCW and SCW CESAs appear to be within distinct complexes. What this means in terms of cellulose quality during this overlapping period is unknown, as the exact biochemical, molecular, and cellular mechanisms that control the differences between PCW and SCW cellulose properties remain to be elucidated (60). Although the interface between PCW and SCWs has yet to be explored with great detail, the overlap between both sets of CESAs could aid in facilitating the contiguous nature of the two wall layers, creating a transition zone between PCWs to SCWs that ensures their structural stability.

We have previously reported that during the peak of SCW formation SCW CSCs have a higher velocity than PCW CSCs under the same imaging conditions (30). However, it has also been reported that, because of both the large variation in observed velocities and the similar means of these velocities, the

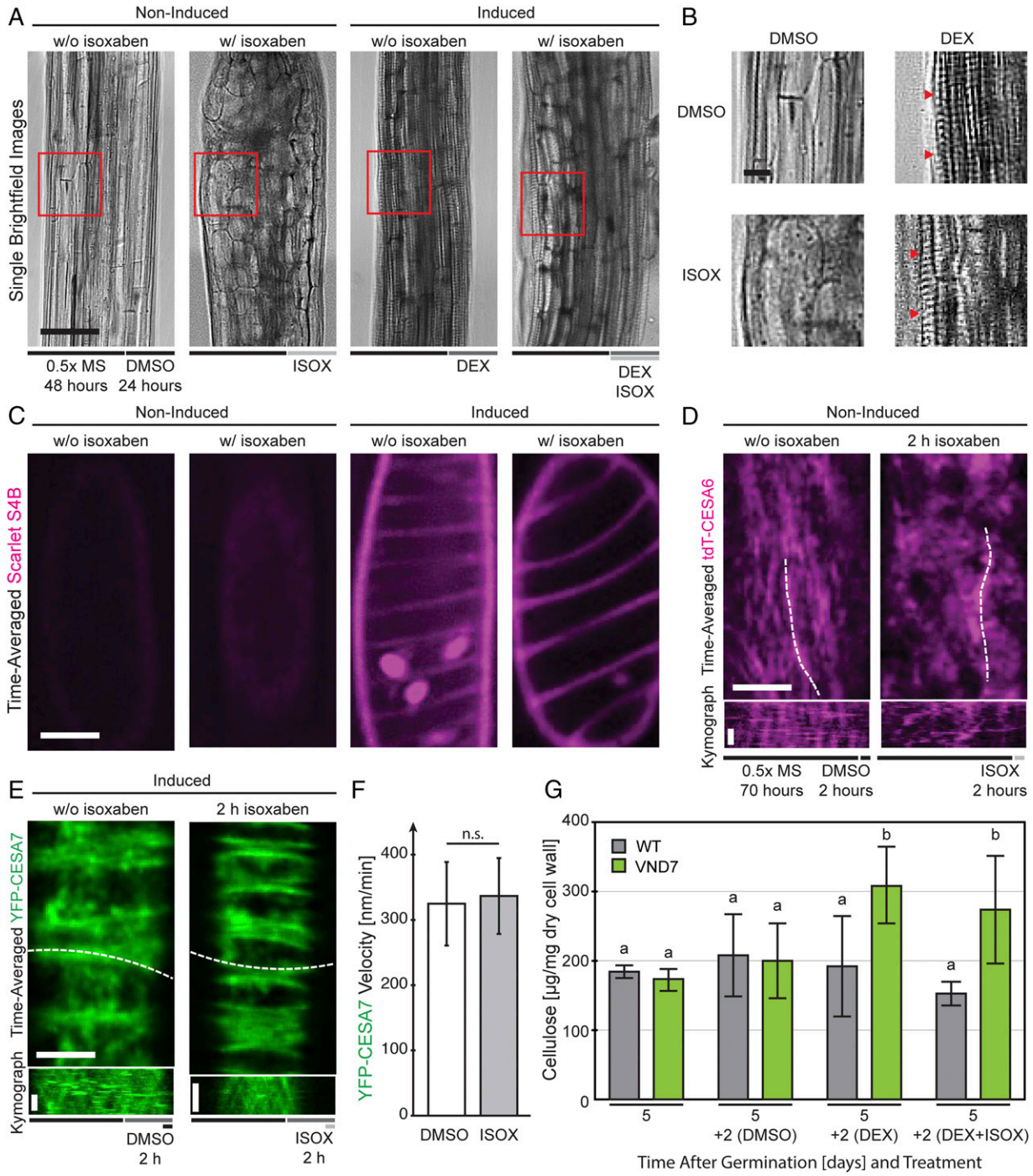

Fig. 4. The potent CESA inhibitor isoxaben affects PCW CESAs but not SCW CESAs during patterned cell wall formation. (*A*) Three-day-old VND7 seedlings grown in the dark for 2 d and transferred to 200 nM isoxaben-containing plates for 1 d were imaged using bright-field illumination. Isoxaben causes the cells of the upper hypocotyl to bulge (compare first and second images from the left). After induction, hypocotyl cells transdifferentiate into protoxylem cells and make SCWs as seen by the striated patterns (third image from the left and *B*). Adding isoxaben to induced seedlings leads to slight bulging of the upper hypocotyl cells while the transdifferentiation is not impaired (fourth image from the left). (Scale bar: 100 μm.) (*B*) Zoomed-in images of the red boxes in *A* showing clear xylem-like cell wall patterns (red arrowheads). (Scale bar: 50 μm.) (*C*) The cellulose stain Scarlet S4B allowed visualization of the secondary wall bands deposited after induction. Noninduced seedlings showed weak and nonspecific labeling (first and second images from the left). Induced seedlings deposit large amounts of cellulose in band patterns in the absence and presence of isoxaben, respectively (third and fourth images from the left). (Scale bar: 10 μm.) (*D*) The effect of isoxaben was analyzed using 3-d-old etiolated double-labeled tdTomato-CESA6 (tdT-CESA6) and YFP-CESA7 seedlings in the VND7-inducible background. Primary wall tdT-CESA6 foci move along linear tracks in the plasma membrane in nontreated (0.5× MS) and noninduced (DMSO) cells but are internalized within 2 h after the addition of 200 nM isoxaben (ISOX) (right image and kymograph below). (Scale bars: 10 μm and 2 min.) (*E*) In contrast, secondary wall YFP-CESA7 foci remain at the plasma membrane and move with similar speeds in both isoxaben and mock-treated cells. (Scale bars: 10 μm and 2 min.) (*F*) Mock-treated (DMSO; $n = 279$) and isoxaben-treated (ISOX; $n = 363$) foci were analyzed; $P > 0.87$, Welch's unpaired t test; n.s, not significant. (*G*) Measurement of the cellulose content of induced and isoxaben-treated induced seedlings compared with nontreated controls of VND7-GR and Col-0 wild-type seedlings reveal that secondary wall production is unaffected by application of isoxaben. Groups were assigned by significant statistical difference based on Welch's unpaired t test ($P < 0.05$ between groups, mean ± SD from three technical and three experimental replicates each).

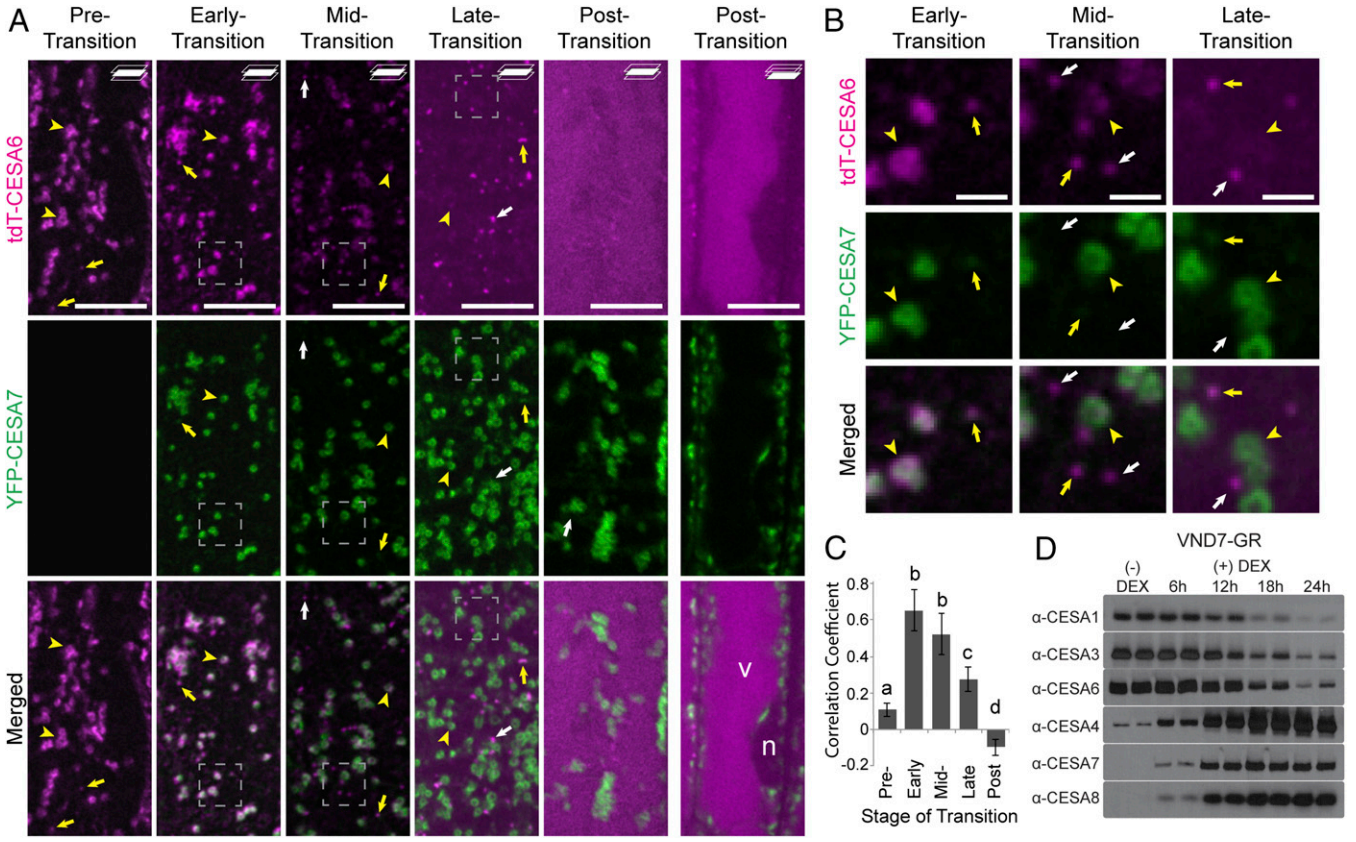

Fig. 5. Primary wall CSCs are trafficked to distinct intracellular compartments and eventually to the vacuole where they are degraded. Shown are 3-d-old etiolated epidermal hypocotyl cells expressing YFP-CESA7 (green) and tdTomato-CESA6 (tdT-CESA6; magenta) in the VND7-inducible background. (*A*) Time course of intracellular signal for tdT-CESA6 and YFP-CESA7 during transition. Pretransition: No YFP-CESA7 signal is observed. Early transition: YFP-CESA7 fluorescence co-occurs with tdT-CESA6 in both Golgi apparatus (arrowheads) and SmaCCs (yellow arrows). Midtransition: Both YFP-CESA7 and tdT-CESA6 signals are seen within Golgi (arrowheads) and SmaCCs (yellow arrows), while tdT-CESA6 fluorescence is also apparent within distinct cortical compartments (white arrows). Late transition: Only YFP-CESA7 signal is seen in Golgi (arrowheads) and SmaCCs while tdT-CESA6 fluorescence is seen as distinct cytosolic puncta (white arrows). Posttransition: tdT-CESA6 is seen only as a diffuse intracellular signal within the vacuole (v), evident at deeper optical planes where the void in fluorescence is caused by the nucleus (n). (Scale bars: 10 μm.) (*B*) Zoomed-in views of the *Insets* in *A* show the differences in localization between tdT-CESA6 and YFP-CESA7 fluorescence within Golgi (arrowheads), SmaCCs (yellow arrows), and bright tdT-CESA6 puncta (white arrows) as transition progresses. (Scale bars: 2 μm.) (*C*) Pearson's correlation coefficient for colocalization of YFP-CESA7 and tdT-CESA6 at the different stages shown in *A*. Means with different letters represent statistically significant differences based on Tukey's pairwise comparison (mean ± SD, $n = 10$ cells from three plants at each stage, $P < 0.05$). (*D*) Western blots of an induction time course of VND7-GR seedlings show that the accumulation of SCW CESAs (CESA4, CESA7, and CESA8) and the degradation of PCW CESAs (CESA1, CESA3, and CESA6) are consistent among CESA isoforms.

differences are not meaningfully different (31). While our observed SCW CSC velocities are within the range of previously reported PCW CSC velocities, the variation between observed velocities may be caused by differences in temperature during imaging. Indeed, CSC velocities have been shown to be highly affected by temperature, e.g., an 8 °C increase in temperature results in a fourfold increase in the velocity of PCW CSCs (22). Because of this temperature phenomenon, we took great care to ensure that imaging conditions between samples were as identical as possible. Furthermore, that we were able in our system to track both PCW and SCW CSCs within the same cell at the same time and still found a significant difference between the ensuing velocities further supports our hypothesis that SCW CSCs have a faster velocity than PCW CSCs. However, until enzymatic assays of CESAs can be carried out in vitro, the difference in enzymatic activity between PCW and SCW CESAs remains to be resolved.

The transition from PCW production to SCW production represents a critical step in plant development and biomass production, involving the complete turnover of the CESA machinery. Although both CSCs make largely the same fundamental product, cellulose, the quality of the end products is significantly different. Generally, cellulose in the SCWs has a higher degree of crystallinity and polymerization (60). While the enzymatic and cellular processes that contribute to and control these polymeric qualities are not fully understood, we outline a comprehensive evaluation of the coordination of PCW and SCW cellulose synthesis during this important process.

Materials and Methods

Generation of Plant Lines. Seeds of *cesa7*$^{irx3\text{-}4}$ plants containing *proCESA7::YFP-CESA7* and *proCaMV35s::VND7-VP16-GR* (30) were crossed with *cesa6*$^{prc1\text{-}1}$ lines containing *proCESA6::tdTomato-CESA6* (36), and F_3 lines homozygous for all three constructs were isolated. Further, plants containing *proCaMV35s::YFP-TUA5* (37) were crossed with *proCaMV35s::VND7-VP16-GR*, and F_3 lines positive for all three constructs were used for imaging.

Seedling Growth and Induction. Seeds were surface sterilized with 20% bleach and 0.1% Triton-X (Sigma-Aldrich) for 5 min and then were washed three times with sterilized distilled water. Seeds were sown on plates containing germination medium [1× MS medium (Phyto Technology Labs), 1% sucrose, 1× Gamborg's Vitamin mix (Sigma-Aldrich), 0.05% MES, and 0.8% agar at pH 5.8]. Plates were wrapped in aluminum foil and were placed at 4 °C for 2 d before being moved into a growth chamber at 21 °C in a vertical position and were grown for 3 d. Plates were then removed from the chamber and under sterile conditions 10 mL of 10 μM dexamethasone (Sigma-Aldrich) in sterilized distilled deionized water was added to the plates for VND7-GR induction. Plates were then rewrapped in

aluminum foil and grown in the dark in a chamber for an additional 8 h (earliest stages of SCW formation) before imaging began. Imaging was carried out between 8 and 18 h following induction. The timing of induction varied slightly among cells in each seedling, so the stage of transition was defined based on either the status of the microtubule array or the presence of YFP-CESA7 signal and the localization of tdTomato-CESA6. The early stages of transition were defined as the time when the YFP-CESA7 signal was detectable only in Golgi, while tdTomato-CESA6 was present both in the Golgi and at plasma membrane. Midtransition was defined as the time when both the YFP-CESA7 signal and the tdTomato-CESA6 signal were present at the plasma membrane. Late transition was defined as the time when only the YFP-ESA7 signal was present at the plasma membrane and the tdTomato-CESA6 signal was seen only in intracellular compartments, including puncta and the vacuole. Posttransition was defined as the time when the tdTomato-CESA6 signal was seen only within the vacuole.

Drug Treatments. For brightfield images, seedlings were grown in the dark for 2 d on 0.5 MS plates and then transferred to media containing 10 μM dexamethasone and/or 200 nM isoxaben (Sigma-Aldrich) and grown in the dark for an additional day. For confocal images of tdT-CESA6 treated with isoxaben, seedlings were first grown on 0.5× MS plates in the dark for 70 h and then transferred into media containing 200 nM isoxaben, and left in the dark for 2 h before being imaged. For confocal images of YFP-CESA7 treated with isoxaben, seedlings were first grown on 0.5× MS plates in the dark for 2 d, then induced with 10 μM dexamethasone in sterilized distilled deionized water for 22 h. Seedlings were then transferred into media containing 200 nM isoxaben, and left in the dark for 2 h before being imaged.

For imaging cellulose, 3-d-old seedlings were incubated in 0.01% Scarlet S4B (Direct Red 23, Sigma-Aldrich) for 10–20 min, were rinsed with water as described (61), and subsequently were imaged.

For the analysis of cell wall content, *proCaMV35s::VND7-VP16-GR* seedlings were dark-grown in liquid 0.5× MS cultures for 5 d and subsequently were treated with DMSO (mock), 10 mM dexamethasone (final concentration, 10 μM), and/or 1 mM isoxaben (final concentration, 200 nM) for another 2 d. Samples were collected after 5 and 7 d.

Wortmannin (Alfa Aesar) was dissolved in DMSO at a stock concentration of 20 mM and was used at a working concentration of 20 μM. Seedlings induced for 10 h were submerged in either 1 mL of 20 μM 0.1% DMSO in 0.5× MS liquid medium or in 0.1% DMSO in 0.5× MS liquid medium, as a control and were placed under gentle vacuum for 5 min to aid drug penetration. Samples were then left at least 30 min (midtransition) or 2 h (late transition) before being imaged. Samples then were washed twice with 0.5× MS liquid medium and were mounted for imaging.

Live-Cell Imaging. Seedlings were mounted between no. 1.5 45 × 40 and 24 × 24 mm coverslips with water and were sealed with silicone vacuum grease.

Imaging for time-course and wortmannin-treatment experiments was performed on two different spinning disk confocal instruments located in the partner laboratories in Vancouver and Melbourne. The former consisted of a Leica DMi8 inverted microscope equipped with a Perkin-Elmer UltraView Yokogawa CSU-X1 spinning-disk system, a Hamamatsu 9100-13-CSU-X1 EMCCD Camera, and a 100× 1.4 NA oil lens. The latter consisted of an inverted Nikon Ti-E microscope equipped with a CSU-W1 spinning disk head (Yokogawa), a deep-cooled iXon Ultra 888 EM-CCD camera (Andor Technology), and an 100× oil-immersion objective (Apo TIRF, NA 1.49). In both cases, YFP was imaged using a 514-nm laser and a 540/30-nm emission filter, while RFP was detected with a 561-nm laser and a 595/50-nm emission filter. Images were captured using the Volocity 6.3 software package (Perkin-Elmer) or MetaMorph (Molecular Devices). The instrument in Melbourne additionally harbored an Andor FRAPPA scanning instrument for photobleaching experiments. Fluorescence recovery after photobleaching (FRAP) was achieved by using a custom-made journal controlling the dual-color imaging (YFP and RFP) and two-color bleaching (100% 514- and 561-nm laser) with MetaMorph software. Typical FRAP settings were 20-μs bleach time per pixel and up to five repetitions resulting in an ∼2- to 5-s exposure to the bleach laser.

Image Analysis. Images were processed using Fiji software (62). Background correction was performed using the subtract background tool with a rolling ball radius of 50 pixels. Occasionally the images had to be drift corrected, which was done with the registration tools inbuilt to Fiji. The velocity of CSCs was measured using open-source FIESTA software (63), which allowed the velocity of moving CSCs to be determined by measuring their slopes in multiple kymograph projections within a short time. Movies were generated using the MtrackJ plugin for Fiji (64) and employ the inbuilt compression codecs in Fiji.

Colocalization Analysis. Colocalization analysis was performed in Volocity 6.3 (Perkin-Elmer) using the colocalization analysis described by Manders et al. (65). The threshold was set to regions of interest (ROIs) drawn in background areas. Individual cells were then selected as ROIs, and correlation coefficients were calculated.

Protein Extraction and Western Blot Analysis. *Arabidopsis* seedlings containing *proCaMV35s::VND7-VP16-GR* were grown in the dark for 4 d on plates before being induced as described above. Two hundred milligrams of seedlings were harvested at each time point (6 h, 12 h, 18 h, and 24 h) along with a DMSO control, which was treated for 24 h as well, and were snap-frozen with liquid nitrogen. Seedlings were then ground to a fine powder and resuspended in acetone containing 10% trichloroacetic acid. Total protein was extracted (66), and protein pellets were resuspended in dilute PBS containing 1% SDS. The protein concentration was assayed using the DC protein assay (Bio-Rad). Samples were then diluted to 2 mg/mL with SDS-loading buffer.

Twenty micrograms of protein were then run on 8% SDS/PAGE gels with a 5% stacking gel and were transferred to a 0.1-um pore nitrocellulose membrane as described (43). Primary antibodies (43, 44) were used at dilutions of 1:2,000 for α-CESA1 and α-CESA4, 1:1,500 for α-CESA6, 1:000 for α-CESA8, 1:700 for α-CESA3, and 1:500 for α-CESA7. Superclonal secondary antibody (goat anti-rabbit IgG; Thermo Fisher Scientific) conjugated with ECL HRP was used at concentrations of 1:30,000 for α-CESA1, 1:20,000 for α-CESA6, 1:15,000 for α-CESA4, αCESA7, and α-CESA8, and 1:10,000 for α-CESA3. The SuperSignal West Pico Chemiluminescent Substrate kit (Thermo Fisher Scientific) and CL-Xposure film (Thermo Fisher Scientific) were used to image Western blots.

Cellulose Analysis. Liquid cultures were harvested after 7 d in the dark. Seedlings were stored in 70% ethanol for 1 wk. To extract cell-wall material, seedlings were first air-dried overnight in a 60 °C oven. The dry material was then frozen in liquid nitrogen and homogenized to a fine powder using metal balls and an oscillating mill (1 min at 25 Hz) from Retsch. The cell-wall powder was washed with pure ethanol and centrifuged at 16,000 × *g* for 10 min. Subsequently, the pellet was resuspended in a 1:1 methanol:chloroform mixture and was centrifuged again at 16,000 × *g* for 10 min. Last, the pellet was resuspended in pure acetone and centrifuged again at 16,000 × *g* for 10 min. Then the cell-wall pellet was air-dried overnight. Approximately 700–800 μg of the dry, insoluble part of the cell wall material were used for further analysis in 2-mL screw-cap tubes. Subsequently, 250 μL of 2 M trifluoroacetic acid was added to the tubes, and the tubes were incubated for 1 h at 121 °C. Afterward, the tubes were supplemented with 300 μL of 2-Propanol (Thermo Fisher Scientific) and left for evaporation under a steady airflow at 40 °C. This step was repeated twice; then the tubes were supplemented with 300 μL distilled water, thoroughly vortexed, and centrifuged at 16,000 × *g* for 15 min. The pellet was further used to determine the amount of crystalline cellulose using the Updegraff method (67).

ACKNOWLEDGMENTS. We thank the University of British Columbia Bioimaging Facility and the Biological Optical Microscopy Platform at the University of Melbourne for technical support; Dr. Ming Tien (Pennsylvania State University) for the gift of the CESA antibodies; and Dr. Taku Demura (Nara Institute of Science and Technology) for seeds of the *35S::VND7-VP16-GR*–inducible system. S.D.M. and A.L.S. received funding support from the Natural Sciences and Engineering Research Council of Canada (NSERC) Discovery Grants program and the NSERC Working on Walls CREATE program. S.P. was funded through Australian Research Council Future Fellowship FT160100218, and R.S. received Computational Biology Research Initiative and Early Career Research Grants from the University of Melbourne. Y.W. was supported by a Natural Sciences and Engineering Research Council of Canada Postgraduate Scholarship-D and a University of British Columbia Four-Year Fellowship Scholarship. J.L.H. was supported by the Center for Lignocellulose Structure and Formation and the Energy Frontier Research Center funded by the Department of Energy Office of Sciences, Basic Energy Sciences under Award DE-SC0001090.

1. McFarlane HE, Döring A, Persson S (2014) The cell biology of cellulose synthesis. *Annu Rev Plant Biol* 65:69–94.
2. Albersheim P, Darvill AG, Roberts K, Sederoff R, Staehelin LA (2011) Plant cell walls: A renewable material resource. *Plant Cell Walls* (Garland Science, New York), 1st Ed, pp 365–405.
3. Gardner KH, Blackwell J (1974) The structure of native cellulose. *Biopolymers* 13: 1975–2001.
4. Atalla RH, VanderHart DL (1984) Native cellulose: A composite of two distinct crystalline forms. *Science* 223:283–285.
5. Delmer DP, Amor Y (1995) Cellulose biosynthesis. *Plant Cell* 7:987–1000.
6. Cosgrove DJ (2005) Growth of the plant cell wall. *Nat Rev Mol Cell Biol* 6:850–861.
7. Schuetz M, Smith R, Ellis B (2013) Xylem tissue specification, patterning, and differentiation mechanisms. *J Exp Bot* 64:11–31.
8. Richmond T (2000) Higher plant cellulose synthases. *Genome Biol* 1:reviews3001.

9. Kimura S, et al. (1999) Immunogold labeling of rosette terminal cellulose-synthesizing complexes in the vascular plant vigna angularis. *Plant Cell* 11:2075–2086.
10. Nixon BT, et al. (2016) Comparative structural and computational analysis supports eighteen cellulose synthases in the plant cellulose synthesis complex. *Sci Rep* 6:28696.
11. Thomas LH, et al. (2013) Structure of cellulose microfibrils in primary cell walls from collenchyma. *Plant Physiol* 161:465–476.
12. Oehme DP, et al. (2015) Unique aspects of the structure and dynamics of elementary Iβ cellulose microfibrils revealed by computational simulations. *Plant Physiol* 168:3–17.
13. Haigler CH, Brown RM (1986) Transport of rosettes from the golgi apparatus to the plasma membrane in isolated mesophyll cells of Zinnia elegans. *Protoplasma* 134: 111–120.
14. Gutierrez R, Lindeboom JJ, Paredez AR, Emons AMC, Ehrhardt DW (2009) Arabidopsis cortical microtubules position cellulose synthase delivery to the plasma membrane and interact with cellulose synthase trafficking compartments. *Nat Cell Biol* 11: 797–806.
15. Crowell EF, et al. (2009) Pausing of Golgi bodies on microtubules regulates secretion of cellulose synthase complexes in Arabidopsis. *Plant Cell* 21:1141–1154.
16. Carpita NC, Delmer DP (1981) Concentration and metabolic turnover of UDP-glucose in developing cotton fibers. *J Biol Chem* 256:308–315.
17. Haigler CH, et al. (2001) Carbon partitioning to cellulose synthesis. *Plant Mol Biol* 47: 29–51.
18. Morgan JLW, Strumillo J, Zimmer J (2013) Crystallographic snapshot of cellulose synthesis and membrane translocation. *Nature* 493:181–186.
19. Paredez AR, Somerville CR, Ehrhardt DW (2006) Visualization of cellulose synthase demonstrates functional association with microtubules. *Science* 312:1491–1495.
20. Diotallevi F, Mulder B (2007) The cellulose synthase complex: A polymerization driven supramolecular motor. *Biophys J* 92:2666–2673.
21. DeBolt S, Gutierrez R, Ehrhardt DW, Somerville C (2007) Nonmotile cellulose synthase subunits repeatedly accumulate within localized regions at the plasma membrane in Arabidopsis hypocotyl cells following 2,6-dichlorobenzonitrile treatment. *Plant Physiol* 145:334–338.
22. Fujita M, et al. (2011) Cortical microtubules optimize cell-wall crystallinity to drive unidirectional growth in Arabidopsis. *Plant J* 66:915–928.
23. Persson S, Wei H, Milne J, Page GP, Somerville CR (2005) Identification of genes required for cellulose synthesis by regression analysis of public microarray data sets. *Proc Natl Acad Sci USA* 102:8633–8638.
24. Persson S, et al. (2007) Genetic evidence for three unique components in primary cell-wall cellulose synthase complexes in Arabidopsis. *Proc Natl Acad Sci USA* 104: 15566–15571.
25. Desprez T, et al. (2007) Organization of cellulose synthase complexes involved in primary cell wall synthesis in Arabidopsis thaliana. *Proc Natl Acad Sci USA* 104: 15572–15577.
26. Taylor NG, Howells RM, Huttly AK, Vickers K, Turner SR (2003) Interactions among three distinct CesA proteins essential for cellulose synthesis. *Proc Natl Acad Sci USA* 100:1450–1455.
27. Carroll A, et al. (2012) Complexes with mixed primary and secondary cellulose synthases are functional in Arabidopsis plants. *Plant Physiol* 160:726–737.
28. Wightman R, Turner S (2010) Trafficking of the cellulose synthase complex in developing xylem vessels. *Biochem Soc Trans* 38:755–760.
29. Yamaguchi M, et al. (2010) VASCULAR-RELATED NAC-DOMAIN6 and VASCULAR-RELATED NAC-DOMAIN7 effectively induce transdifferentiation into xylem vessel elements under control of an induction system. *Plant Physiol* 153:906–914.
30. Watanabe Y, et al. (2015) Visualization of cellulose synthases in Arabidopsis secondary cell walls. *Science* 350:198–203.
31. Li S, et al. (2016) Cellulose synthase complexes act in a concerted fashion to synthesize highly aggregated cellulose in secondary cell walls of plants. *Proc Natl Acad Sci USA* 113:11348–11353.
32. Schneider R, et al. (2017) Two complementary mechanisms underpin cell wall patterning during xylem vessel development. *Plant Cell* 29:2433–2449.
33. Schuetz M, et al. (2014) Laccases direct lignification in the discrete secondary cell wall domains of protoxylem. *Plant Physiol* 166:798–807.
34. Yamaguchi M, et al. (2011) VASCULAR-RELATED NAC-DOMAIN7 directly regulates the expression of a broad range of genes for xylem vessel formation. *Plant J* 66:579–590.
35. Li Z, Fernie AR, Persson S (2016) Transition of primary to secondary cell wall synthesis. *Sci Bull (Beijing)* 61:838–846.
36. Sampathkumar A, et al. (2013) Patterning and lifetime of plasma membrane-localized cellulose synthase is dependent on actin organization in Arabidopsis interphase cells. *Plant Physiol* 162:675–688.
37. Kirik A, Ehrhardt DW, Kirik V (2012) TONNEAU2/FASS regulates the geometry of microtubule nucleation and cortical array organization in interphase Arabidopsis cells. *Plant Cell* 24:1158–1170.
38. Scheible W-R, Eshed R, Richmond T, Delmer D, Somerville C (2001) Modifications of cellulose synthase confer resistance to isoxaben and thiazolidinone herbicides in Arabidopsis Ixr1 mutants. *Proc Natl Acad Sci USA* 98:10079–10084.
39. Brabham C, Stork J, Barrett M, DeBolt S (2018) Grass cell walls have a role in the inherent tolerance of grasses to the cellulose biosynthesis inhibitor isoxaben. *Pest Manag Sci* 74:878–884.
40. Anderson CT, Carroll A, Akhmetova L, Somerville C (2010) Real-time imaging of cellulose reorientation during cell wall expansion in Arabidopsis roots. *Plant Physiol* 152: 787–796.
41. Fujimoto M, Suda Y, Vernhettes S, Nakano A, Ueda T (2015) Phosphatidylinositol 3-kinase and 4-kinase have distinct roles in intracellular trafficking of cellulose synthase complexes in Arabidopsis thaliana. *Plant Cell Physiol* 56:287–298.
42. Robinson DG, Jiang L, Schumacher K (2008) The endosomal system of plants: Charting new and familiar territories. *Plant Physiol* 147:1482–1492.
43. Hill JL, Jr, Hammudi MB, Tien M (2014) The Arabidopsis cellulose synthase complex: A proposed hexamer of CESA trimers in an equimolar stoichiometry. *Plant Cell* 26: 4834–4842.
44. Hill JL, Jr, Josephs C, Barnes WJ, Anderson CT, Tien M (2018) Longevity in vivo of primary cell wall cellulose synthases. *Plant Mol Biol* 96:279–289.
45. Korbei B, Luschnig C (2013) Plasma membrane protein ubiquitylation and degradation as determinants of positional growth in plants. *J Integr Plant Biol* 55:809–823.
46. Abas L, et al. (2006) Intracellular trafficking and proteolysis of the Arabidopsis auxin-efflux facilitator PIN2 are involved in root gravitropism. *Nat Cell Biol* 8:249–256, and erratum (2006) 8:424.
47. Kasai K, Takano J, Miwa K, Toyoda A, Fujiwara T (2011) High boron-induced ubiquitination regulates vacuolar sorting of the BOR1 borate transporter in Arabidopsis thaliana. *J Biol Chem* 286:6175–6183.
48. Carroll A, Specht CDD (2011) Understanding plant cellulose synthases through a comprehensive investigation of the cellulose synthase family sequences. *Front Plant Sci* 2:5.
49. Chen S, Ehrhardt DW, Somerville CR (2010) Mutations of cellulose synthase (CESA1) phosphorylation sites modulate anisotropic cell expansion and bidirectional mobility of cellulose synthase. *Proc Natl Acad Sci USA* 107:17188–17193.
50. Chen S, et al. (2016) Anisotropic cell expansion is affected through the bidirectional mobility of cellulose synthase complexes and phosphorylation at two critical residues on CESA3. *Plant Physiol* 171:242–250.
51. Sánchez-Rodríguez C, et al. (2017) BRASSINOSTEROID INSENSITIVE2 negatively regulates cellulose synthesis in *Arabidopsis* by phosphorylating cellulose synthase 1. *Proc Natl Acad Sci USA* 114:3533–3538.
52. Bischoff V, et al. (2011) Phytochrome regulation of cellulose synthesis in Arabidopsis. *Curr Biol* 21:1822–1827.
53. Taylor NG (2007) Identification of cellulose synthase AtCesA7 (IRX3) in vivo phosphorylation sites–A potential role in regulating protein degradation. *Plant Mol Biol* 64:161–171.
54. Bashline L, Li S, Gu Y (2014) The trafficking of the cellulose synthase complex in higher plants. *Ann Bot* 114:1059–1067.
55. Leitner J, et al. (2012) Lysine63-linked ubiquitylation of PIN2 auxin carrier protein governs hormonally controlled adaptation of Arabidopsis root growth. *Proc Natl Acad Sci USA* 109:8322–8327.
56. Viotti C, et al. (2010) Endocytic and secretory traffic in Arabidopsis merge in the trans-Golgi network/early endosome, an independent and highly dynamic organelle. *Plant Cell* 22:1344–1357.
57. Sanderfoot AA, Kovaleva V, Bassham DC, Raikhel NV (2001) Interactions between syntaxins identify at least five SNARE complexes within the Golgi/prevacuolar system of the Arabidopsis cell. *Mol Biol Cell* 12:3733–3743.
58. Dettmer J, Hong-Hermesdorf A, Stierhof YD, Schumacher K (2006) Vacuolar H^+-ATPase activity is required for endocytic and secretory trafficking in *Arabidopsis*. *Plant Cell* 18: 715–730.
59. Ueda T, Yamaguchi M, Uchimiya H, Nakano A (2001) Ara6, a plant-unique novel type Rab GTPase, functions in the endocytic pathway of Arabidopsis thaliana. *EMBO J* 20: 4730–4741.
60. Joshi CP, Mansfield SD (2007) The cellulose paradox–Simple molecule, complex biosynthesis. *Curr Opin Plant Biol* 10:220–226.
61. Liesche J, Ziomkiewicz I, Schulz A (2013) Super-resolution imaging with Pontamine Fast Scarlet 4BS enables direct visualization of cellulose orientation and cell connection architecture in onion epidermis cells. *BMC Plant Biol* 13:226.
62. Schindelin J, et al. (2012) Fiji: An open-source platform for biological-image analysis. *Nat Methods* 9:676–682.
63. Ruhnow F, Zwicker D, Diez S (2011) Tracking single particles and elongated filaments with nanometer precision. *Biophys J* 100:2820–2828.
64. Meijering E, Dzyubachyk O, Smal I (2012) Methods for cell and particle tracking. *Methods Enzymol* 504:183–200.
65. Manders EMM, Verbeek FJ, Aten JA (1993) Measurement of co-localization of objects in dual-colour confocal images. *J Microsc* 169:375–382.
66. Wang W, Vignani R, Scali M, Cresti M (2006) A universal and rapid protocol for protein extraction from recalcitrant plant tissues for proteomic analysis. *Electrophoresis* 27: 2782–2786.
67. Updegraph DM (1969) Semi-micro determination of cellulose in biological materials Anal. *Biochem Anal Biochem* 32:420–424.